Article

Not peer-reviewed version

The Agricultural Application of Full Polar and Quantification S-band SAR Subsystem of Chinese High-Resolution Aerial Remote Sensing System

Yabo Liu * , Luhao Wang , Shuang Zhu , Xiaojie Zhou , Jia Liu

Posted Date: 13 October 2023

doi: 10.20944/preprints202310.0900.v1

Keywords: Full polarimetric SAR; S-band; Agricultural application; Quantification

Article

The Agricultural Application of Full Polar and Quantification S-Band SAR Subsystem of Chinese High-Resolution Aerial Remote Sensing System

Yabo Liu [1,*], Luhao Wang [1,2], Shuang Zhu [1,2], Xiaojie Zhou [3] and Jia Liu [4]

[1] Aerospace Information Research Institute, Chinese Academy of Sciences, Beijing, 100094, China; wangluhao22@mails.ucas.ac.cn (L.W.); zhushuang21@mails.ucas.ac.cn (S.Z.)
[2] School of Electronic, Electrical and Communication Engineering, University of Chinese Academy of Sciences, Beijing, 100049, China
[3] School of Electronic Information Engineering, University of Beihang, Beijing, 100083, China; zhouxiaojie0730@buaa.edu.cn (X.Z.)
[4] Institute of Agricultural Resources and Regional Planning, Chinese Academy of Agricultural Sciences, Beijing, 100089, China; Liujia06@cass.cn (J.L.)
* Correspondence: liuyb@aircas.ac.cn (Y.L.)

Abstract: Based on the high-precision quantitative measurement ability, the S-band subsystem of China's high-resolution aviation system carried out the agricultural application test for the first time in Jilin elm, China. The experiment is mainly carried out in combination with vegetation growth, soil moisture content inversion, wheat straw returning and ground feature classification. Through the design of quantitative measurement scheme, the results of different straw coverage and observation at different times are compared, which shows the prospect of S-band full polarization synthetic aperture radar system in the field of agricultural application.

Keywords: full polarimetric SAR; S-band; agricultural application; quantification

1. Introduction

1.1. The current situation of black land in Northeast China and the demand of microwave remote sensing

Northeast China is one of the world's four major black soil areas, with a total area of about 1.03 million square kilometers, a typical black soil area of about 170,000 square kilometers, and an annual production of about 22.5 billion to 25 billion kilograms of commodity grain, which plays an important role in China's agricultural development, especially in food production. Moisture in the soil of northeast black soil is the main source of plant and crop survival, which determines the height of plants and the development of crop root system, which is very important to the formation of yield. As China's main corn-producing area, straw field, as an important part of farmland ecosystem, affects the flow and circulation of nutrients, carbon, water and energy in farmland ecosystem, and has important value in agricultural production and soil fertilization. As a national grain silo, the plant species cultivated in the black land of Northeast China, the development, growth status and area monitoring are of great significance for estimating grain yield. After many years of development and reclamation, the black land in Northeast China is faced with soil erosion and ecological environment deterioration, the organic matter content in the soil is now nearly two-thirds lower than before reclamation, the phenomenon of plate knots and salinization are serious, and it is urgent to carry out the protection of cultivated land.

Remote sensing information has the characteristics of large coverage, short observation period and high timelines. The use of remote sensing images to monitor the proportion of straw covered fields after crop harvest and the new season after crop seeding, crop growth and crop estimation is not only low cost, efficiency and precision are greatly improved, but also an important technical mean to influence soil moisture, organic matter and physical and chemical properties after the implementation of conservation farming and follow-up research on straw return to the field[1]. Optical

 doi:10.20944/preprints202310.0900.v1

agricultural remote sensing is early, the remote sensing mechanism and technology are relatively mature, is the main agricultural remote sensing method, but it is vulnerable to cloud rain, fog, haze and other environmental impact, can not obtain continuous Earth observation data. Microwave remote sensing can obtain high-resolution observation images of areas of interest all day long, continuous monitoring during the critical period of crop growth season, exploration of electromagnetic waves and the interaction between earth and environment, provide theoretical basis for soil carbon nitrogen cycle, and is conducive to soil moisture, oxygen and organic matter survey, guide agricultural production and crop biomass monitoring, has become an important way of agricultural remote sensing.

1.2. Research on the application of SAR remote sensing in agriculture

Synthetic Aperture Radar(SAR), because of the polarization characteristics of its data, the backward scattering intensity and the sensitivity of phase characteristics to soil moisture, it has a unique detection ability for water-related information identification, which can play a role that other remote sensing means are difficult to play, and become one of the most effective methods in high spatial resolution soil moisture monitoring[2-5].

Straw returning is mainly monitored by crop residue cover (CRC). Narayanan et al. estimated corn CRC using multi-band microwave scattering meters, and found that the radar backward scattering coefficient had a good linear relationship with corn CRC. The residual coverage of corn was estimated using X-band microwave scattering data, with an average estimation error of 13% and 8% based on horizontal and vertical polarization data[6]. McNairn et al. fitted different crop residual coverage in different soil backgrounds with the backward scattering coefficient of Radarsat-1 standard pattern data (R2=0.53), estimated the residual coverage of crops such as wheat, corn and soybeans, and found that the estimation error of wheat and rice was large and the relative error of corn and soybean was small[7]. McNairn et al. also analyzed the relationship between SAR data of different polarization methods and corn residual coverage, and found that only the backward scattering coefficient of HV polarization method had significant correlation with corn residual coverage[8]. The existing statistical method based on radar data simply analyzes the backward scattering coefficient and crop residual coverage, which has great regional limitations. With the development of microwave remote sensing technology, more information (polarization information, phase information, etc.) is introduced into the monitoring of crop residue coverage, and the accuracy of estimation will be significantly improved by introducing radiation transmission model into crop residue coverage monitoring.

In the use of polarized information, mainly for the classification of earth matter. Li et al. analyzed the change of scattering mechanism in rice growth with the polarization decomposition characteristics of 4-scene Radarsat-2 fully polarized images, and used SVM classifiers to extract the fully polarized SAR rice planting area, and the results show that the polarization decomposition characteristics can obtain better classification results than linear backward scattering coefficients [9, 10]. McNairn et al. used multi-phase optical images and SAR images to classify crops based on decision trees [11], In addition, the classification and monitoring of corn and soybeans were carried out using TerraSAR-X and Radarsat-2 data from pre-growth crops [12]. Xu et al. discussed the relationship between the polarization decomposition characteristics of wheat planting area and the change of growth cycle with the multi-phase full polarization image, and combined the backward scattering coefficient with the polarization decomposition feature to realize the extraction of wheat region [13]. Jiao et al. classified the 19-scene Radarsat-2 images based on objects, and the experimental results showed that Freeman-Durden decomposition and Cloude decomposition had some advantages over linear backward scattering coefficients [14]. Kenduiywo et al. proposed a multi-phase SAR classification method based on dynamic conditions with the airport to realize the comprehensive utilization of spatial information and multi-time phase information[15], The HH/VV bipolarization data of TerraSAR-X were verified. Li et al. used UAVSAR data to monitor and classify the scattering characteristics of major crops in the Sacramento Valley region of California, U.S.A[16].

Preprints (www.preprints.org) | NOT PEER-REVIEWED | Posted: 13 October 2023 doi:10.20944/preprints202310.0900.v1

1.3. High Resolution Aviation System S-band Radar Introduction

The multi-dimensional synthetic aperture radar (SAR)[17] developed by the Chinese high resolution aviation system project quantifies targets in multiple dimensions, including multi-band, multi-polarization, multi-temporal, and multi-angle to obtain more complete target characteristics for scientific research and quantitative remote sensing applications in various fields. The Institute of Space and Astronautics, CAS, is an overall multi-dimensional project responsible for developing C-band and S-band radar subsystems. Among them, the S-band fully polarized SAR system completed the trial sample acceptance in December 2018, and the quantitative indexes of the system are: relative radiation accuracy better than 1 dB, absolute radiation accuracy better than 2.5 dB, polarization phase imbalance ≤ 5, amplitude imbalance: ≤ 1 dB (1σ), and planar geometric positioning accuracy better than 5 m. With the high-resolution special application demonstration project funding, the first agricultural observation application experiment was conducted in the Yushu area of Jilin Province, China, from May 24 to 27, 2020. The main objective of the experiment is: to carry out the first quantitative application of airborne S-band SAR polarization and radiation in China through precise calibration of the system. To study the demonstration applications in agriculture, forestry, grassland, wetland and water surface observation, feature classification, and straw field cover[18-23]. In addition, the ability of S-band SAR to reflect changes in soil water content and crop growth is explored through multi-temporal observations, and the interaction law between S-band electromagnetic waves and landforms is further explored. The S-band RCS characteristic curves of different features were established through multi-angle observation, and the relationship between the polarization scattering characteristic matrix and the observation angle was analyzed[24].

The structure of this paper is designed as follows, firstly, the S-band radar subsystem of the high-resolution aerial system is introduced in general. The flight program in the Yushu area is designed, including the calibration flight and the agricultural observation test, and the quantitative index of the system is measured. The RCS data and the polarization scattering characteristic matrix of the features used in this flight are obtained. Finally, the preliminary research results of S-band radar in terms of characteristic backscattering coefficient statistics, straw cover, soil moisture, and crop classification are given using multi-temporal and multi-polarized multi-dimensional quantitative information.

1.4. High Resolution Aviation System S-band Radar Subsystem Introduction And Processing Effect

The multi-dimensional synthetic aperture radar of the Chinese high resolution aerial system quantifies the target in multi-band, multi-polarization, multi-temporal, elevation, multi-angle, and other multi-dimensions, which can obtain more complete target characteristics for scientific research and quantitative remote sensing applications in various fields. The S-band radar subsystem is one of the six single-band radar subsystems designed and deployed in the multi-dimensional SAR system, which can provide quantitative measurement information such as full polarization, multi-temporal phase, and scattering coefficient.

1.4.1. System composition and main functions

There are two support states for the S-band radar subsystem. The first support state is a multi-dimensional radar system subsystem that works jointly with one or more other band radar subsystems under the centralized control of the multi-dimensional radar system. The second support state is that the S-band radar subsystem works independently as a radar.

When working jointly, the multi-dimensional radar provides a unified mission management computer, data logger, real-time imaging processor, and motion attitude measurement equipment with a unified mounting cabinet. In this matched state, the S-band radar subsystem consists of three components: an antenna unit, an integrated electronics unit, and a power distribution unit. The system composition, the interconnection relationship between the units and the external interfaces of the system are shown in the following figure. The antenna unit is installed under the belly of the wheel loader, and the power distribution unit and the integrated electronics unit are installed in the cabin of the wheel loader.

Preprints (www.preprints.org) | NOT PEER-REVIEWED | Posted: 13 October 2023 doi:10.20944/preprints202310.0900.v1

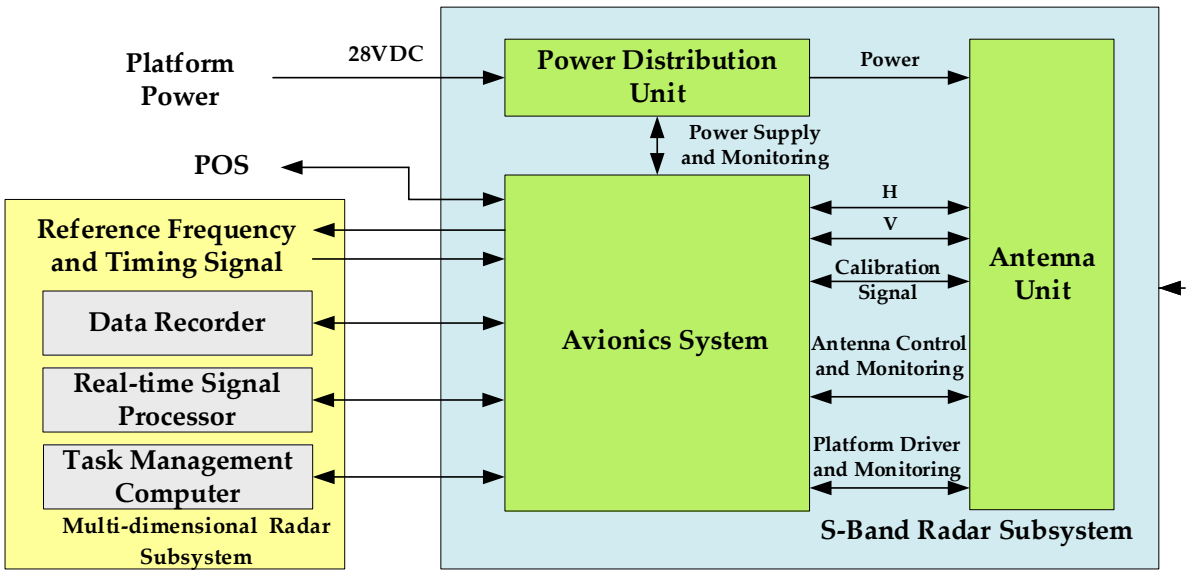

Figure 1. System composition of multi-dimensional joint work.

The S-band radar is a complete synthetic aperture radar when the single band works independently. The system composition includes antenna unit, integrated electronics unit, power distribution unit, mission management unit, data recording unit, signal processing unit, motion attitude measurement equipment, and cabinet. The system composition, the interconnection relationships between the units, and the external interfaces of the system are shown in the following figure. The antenna unit is installed under the belly of the wheel loader, and the other equipment is installed in the wheel loader cabin.

1.4.2. System main technical requirement

The following table shows the technical indexes achieved by the S-band radar subsystem.

Table 1. Technical indexes.

Parameters	Value
Operating frequency	S, Center Frequency 3.2Ghz
Operating pattern	Full polarimetric stripmap mode
Polarization	HH,HV,VH,VV
Resolution/ Swath width / Operating distance	1m/15km/20km
Operating range	1000 ~ 10000m
Polarization isolation	≥ 28dB(Antenna) ≥ 30 dB (Corner reflector)
Noise equivalent sigma zero	-30dB (20km Operating distance, 1m Resolution) ≤-33dB (30km Operating distance, 3m Resolution) ≤ -35dB (40km Operating distance, 10m Resolution)
Side-lobe level and ambiguity	ISLR ≤ -13Db; PSLR: ≤ -20dB; Azimuth ambiguity≤ -20dB; Range ambiguity≤ -20dB
Quantitative measurement index	
Geometric measurement accuracy	Horizontal accuracy ≤ 5m (1σ) (Flatland DEM)
Relative radiometric calibration	≤ 1dB（3σ）
Absolute radiometric calibration	≤ 2.5dB（3σ）

 doi:10.20944/preprints202310.0900.v1

Polarimetric imbalances	Phase ≤ 5°（1σ） Amplitude：≤ 1dB（1σ）

Note: ISLR: Integral sidelobe ratio; PSLR: Peak side lobe ratio.

2. Materials and Methods

From 24 to 27 May 2020, the agricultural observation experiment was carried out using the S-band radar subsystem carried on the small to medium-sized platform of Sesner 208B. Yushu City is located in the world-famous Golden Corn Belt with fertile land, which is the national key commodity grain base, and the preferred place for the deployment of monitoring points. From May to June each year, the local area is at the stage of corn budding. During this period, it is of typical demonstration significance to use S-band radar remote sensing technology to monitor soil moisture, straw returning and black soil conservation in these areas, thereby providing a basis for subsequent large-scale remote sensing applications.

The area covered by this application-calibration flight survey is about 700 square kilometers. The coordinates of the surveyed area are shown in the Table 2

Table 2. Four-point coordinates of Jilin Yushu survey area.

Vertex	Longitude	Latitude
S1	126.46331	45.171747
S2	126.475753	44.823366
S3	126.707185	44.825671
S4	126.697717	45.173504

This quantitative scheme adopts the observation mode of air-ground collaboration. In terms of flight test, considering that S-band radar will be installed on a new aircraft, external calibration flight is needed before formal agricultural observation to calibrate the performance of the system. In view of the observation of soil moisture and crop growth, it is necessary to conduct observation in different time phases. In ground survey, multiple ground observation points are selected evenly in the survey area, including bare land, the land covered by straw, corn field at germination stage, wetland, water surface and other geophysical environment conditions. The survey crew measures soil water content, oxygen content and organic matter, coverage of returned straw, crop growth and other crop growth parameters at the time of flight observation.

According to the above analysis, this experiment uses two flights of different dates to complete the multi-temporal observation task required by agricultural purpose. Among the two flights, 1/3 voyage of the first flight is used as calibration flight outside the airport, and the rest is then used for the agricultural observation experiment in the survey area. The second flight is only used for agricultural observation experiment.

2.1. Route planning

The white area in the figure refers to the area to be surveyed, and the yellow mark represents the airport where the aircraft takes off and lands.

Preprints (www.preprints.org) | NOT PEER-REVIEWED | Posted: 13 October 2023 doi:10.20944/preprints202310.0900.v1

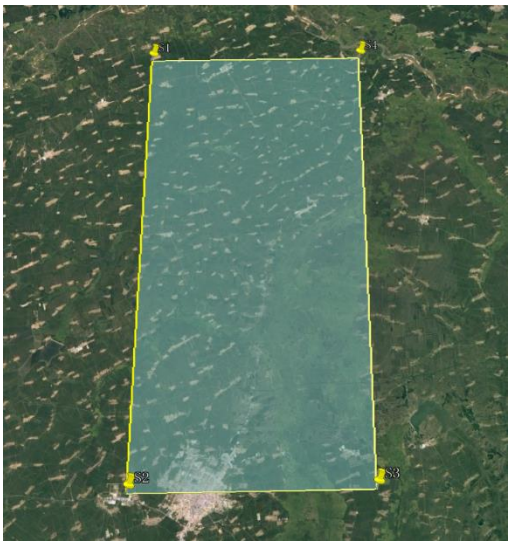

Figure 2. Route planning.

The flight task is divided into two tasks, i.e., calibration flight and survey area flight. The introduction to each task is shown:

Table 3. Introduction to the calibration flight.

Index	Calibration flight	Task introduction
Task date	2020.0524	2020.0524\0527
Survey area	Jilin Yushu	Jilin Yushu
Side visual angle	45° (Left view)	45° (Left view)
Flight altitude	2200m	4200m
Flight speed	250km/h	250km/h
Breadth	1456m	4000m
Lateral overlapping degree	\	30%
Lateral extension	\	20%
Mean height of survey area	\	200

The planned route is as follows:

Preprints (www.preprints.org) | NOT PEER-REVIEWED | Posted: 13 October 2023 doi:10.20944/preprints202310.0900.v1

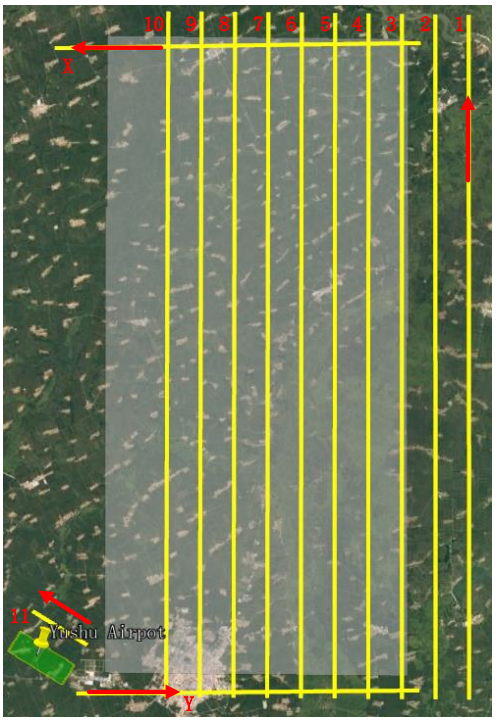

Figure 3. Route diagram.

In the diagram, the routes from 1 – 10 are used to cover the survey area, and the average length of each route is between 40 km and 41 km. The length of the straight line needed by a flight to cover the survey area is 410 km, and the covered area is 1600 square kilometers (including the overlapping part). Route 11 is used for calibration flight, and X, Y is the framework route. The pilot data table is as follows:

Table 4. Route diagram.

Route No.	Start		Destination	
	Longitude	Latitude	Longitude	Latitude
1	126°45′18.10″	126°45′18.10″	126°45′18.10″	126°45′18.10″
2	126°43′45.35″	44°48′46.74″	126°43′05.23″	45°11′14.54″
3	126°42′12.60″	44°48′45.92″	126°41′31.86″	45°11′13.93″
4	126°40′39.84″	44°48′45.07″	126°39′58.49″	45°11′13.32″
5	126°39′07.09″	44°48′44.22″	126°38′25.12″	45°11′12.68″
6	126°37′34.34″	44°48′43.32″	126°36′51.76″	45°11′12.02″
7	126°36′01.59″	44°48′42.41″	126°35′18.39″	45°11′11.33″
8	126°34′28.84″	44°48′41.50″	126°33′45.03″	45°11′10.64″
9	126°32′56.09″	44°48′40.54″	126°32′11.67″	45°11′09.90″
10	126°31′23.35″	44°48′39.57″	126°30′38.34″	45°11′08.37″
11	126°25′08.42″	44°51′20.83″	126°27′41.62″	44°50′17.40″
Y	126°27′15.83″	44°48′41.86″	126°42′59.94″	44°49′03.59″
X	126°42′26.27″	45°10′17.20″	126°25′23.49″	45°09′50.42″

Considering that the flight time of general aviation aircraft is about 5 hours per flight, and the effective operation time is 3 hours, the effective flight mileage is 750 km. A single flight can meet the

 doi:10.20944/preprints202310.0900.v1

requirements to observe the entire survey area, and two flights are available to complete two cover flights in different time phases for the survey area.

2.2. Design of External Calibration Field and Determination of Quantitative Index

2.2.1. Design of External Calibration Field

Before carrying out agricultural application experiments, external calibration flight inspection is required. The purpose of calibration flight experiment is to exam the system function and performance index, survey resolution, side lobe ratio, radiation calibration accuracy, polarization calibration accuracy and other quantitative indexes by using external calibration method. Therefore, the external calibration equipment used for the flight test is also an important test equipment for this flight test. The calibration field test equipment includes the calibrator and other equipment required to install and test the calibrator at the external field. The test equipment at the calibration field for the S-band radar subsystem flight test is shown in the following table:

Table 5. Test equipment at calibration field.

No.	Description	Qty.	Remarks
1	0° dihedral corner reflector (Side length of 0.6m)	3	For polarization calibration
2	22.5° dihedral corner reflector (Side length of 0.6m)	2	
3	45° dihedral corner reflector (Side length of 0.6m)	1	
7	trihedral angle reflector (Right-angle side length of 0.7m)	13	For resolution measurement and radiation calibration mode
8	Difference measurement equipment	1 set	Measure the position of aerial carrier and the corner reflector

The calibration experiment field site is selected and set at a large area with flat terrain and weak ground-object backscattering. The following figure shows the layout diagram of calibration field angle reflector.

Preprints (www.preprints.org) | NOT PEER-REVIEWED | Posted: 13 October 2023 doi:10.20944/preprints202310.0900.v1

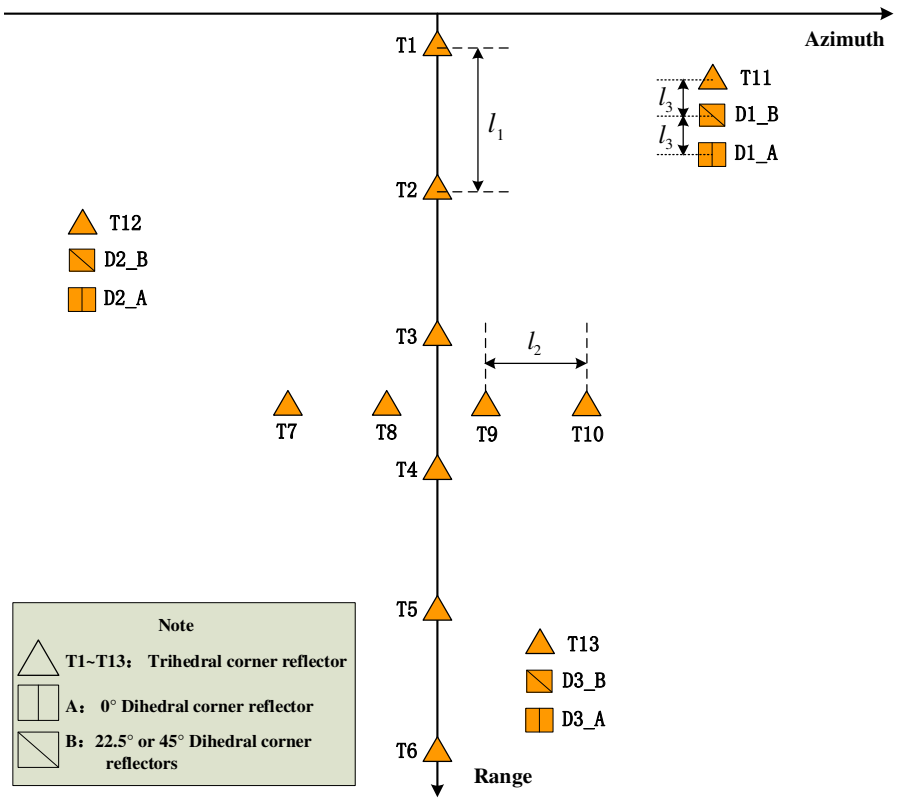

Figure 4. Layout diagram of calibration field.

In the diagram, T1-T6 are used for radar range radiation calibration, which should be uniformly distributed in the mapping bandwidth, and l1 is calculated accordingly. T7-T10 are used for azimuth radiation calibration, and l2 is not less than 100 meters. T11-T13 and D1-D3(A/B) are used for polarization calibration, and l3 is not less than 200 meters. When deploying the calibrator, it is necessary to overlap the normal line of each calibrator with the connection line between the calibrator and the aircraft in the front and side view.

The ground synchronous data acquisition scheme requires the difference measurement equipment to synchronize, during the flight of the aircraft, the position information of the aircraft and the calibrator, thereby obtaining high-precision relative position relationship.

Relevant radar and flight parameters are shown in Table 6.

Table 6. Radar and flight parameters.

Parameter	Value
Ground elevation（m）	200
Calibration flight elevation（m）	2200
Local elevation（m）	200
Flight speed（m/s）	70
View-angle coverage（°）	27-53
Sampling frequency（MHz）	400
Wave length（m）	0.09375
Average power（w）	19.2w
Receiver gain（dB）	67

Preprints (www.preprints.org) | NOT PEER-REVIEWED | Posted: 13 October 2023 doi:10.20944/preprints202310.0900.v1

2.2.2. Determination of Quantitative Index

1. Resolution

The selected calibration field is near the runway in the airport. The ground object of the airport is bare land, and six trihedral corner reflectors are arranged with the interval of 300 m. The following figure shows the SAR image of the calibration field and the two-dimensional profile of the calibrator.

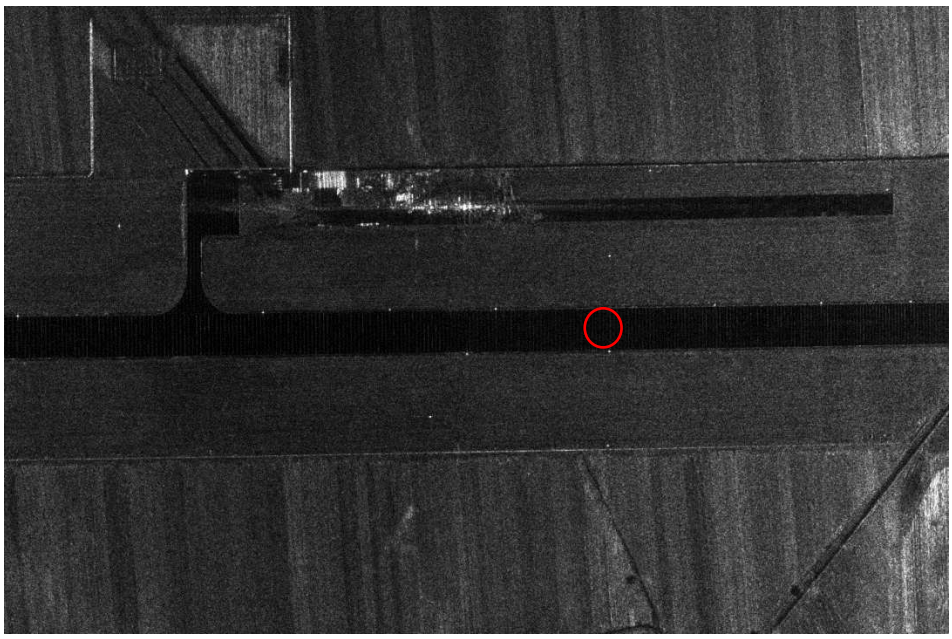

Figure 5. Calibration field imaging result.

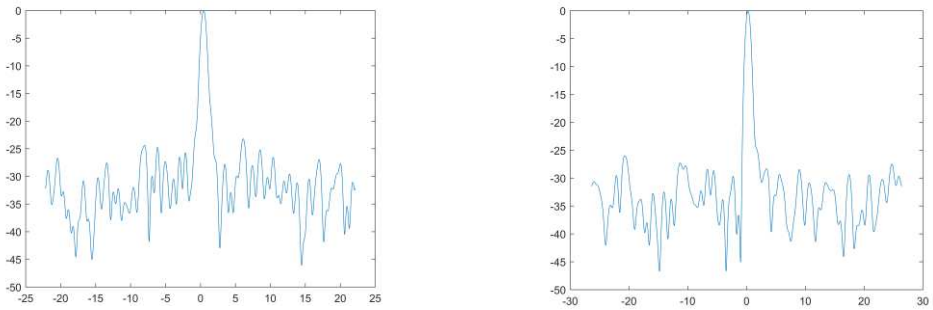

(a) **(b)**

Figure 6. Mode 1 (1m) resolution point target corresponding (midrange) (a)Azimuth (b)Range.

It can be seen from the measurement resolution index of multiple calibrators navigated that in the whole breadth, both the image distance and azimuth resolution are better than 1 m, the peak side lobe ratio is better than 20 dB, and the integral side lobe ratio is better than 15 dB.

1. Radiometric Calibration

Relative radiation accuracy is a measure of system stability, which refers to the maximum error of the relative value of target backscatter coefficient or radar cross-sectional area measured at different positions in the SAR image. Usually, the maximum error value is expressed in dB, and its calculation formula is shown:

$$\Delta_{rad\_r} = \sqrt{\sum_{i=1}^{N_p} \frac{\left(\hat{\varepsilon}_{idB} - \overline{\varepsilon}_{dB}\right)}{N_p}} \quad (1)$$

Preprints (www.preprints.org) | NOT PEER-REVIEWED | Posted: 13 October 2023 doi:10.20944/preprints202310.0900.v1

In the formula, $\hat{\varepsilon}_{idB}$ is the point target energy of the i inspection point expressed in dB, and $\overline{\varepsilon}_{dB}$ is the average value of the point target energy of N_p inspection points, and its calculation formula is as follows:

$$\overline{\varepsilon}_{dB} = \frac{1}{N_p}\sum_{i=1}^{N_p}\hat{\varepsilon}_{idB} \tag{2}$$

Absolute radiation accuracy refers to the error between the measured value of the backscatter coefficient of a uniform target on the ground or the radar cross-sectional area of a point target on the SAR image and the actual value of the target's backscatter coefficient or radar cross-sectional area. Typically, the maximum error value is expressed in dB. The absolute radiation accuracy reflects the absolute difference between the backscatter coefficient or radar cross-sectional area of the ground object corresponding to the image pixel after radiometric calibration and the backscatter coefficient or radar cross-sectional area of the real ground object. Its calculation formula is shown by formula (3):

$$\Delta_{rad\_a} = \max\left\{\left|\hat{\sigma}_i - \sigma_i\right|\right\} \tag{3}$$

In the formula, $\hat{\sigma}_i$ is the RCS measurement value (dBm²) of the i inspection point, and σ_i is the nominal RCS measurement value (dBm²) of the i inspection point.

To verify the performance of the system in complex environments, the radiation calibration process only corrects the effects of the cubic term of the antenna pattern and distance. The point target energy of the index inspection point (corner reflector) ε_P is calculated using the peak value method. The amplitude of the peak point in the energy sub-image corresponding to the inspection point is taken as the energy of the inspection point ε_P. It can be seen from the measurement indicators of multiple calibrators that have been voyaged many times, the relative radiation accuracy is better than 1dB and the absolute radiation accuracy is better than 2.5dB in the entire width range.

2. Polarization Calibration

Polarization isolation refers to the ratio of the energy of the transmitted or received H-polarized (V-polarized) signal to the energy of the serially transmitted or received V-polarized (or H-polarized) signal. The calculation formula of polarization isolation is as follows:

$$\Delta_{pol1} = 20\cdot\lg\left(\min\left\{\sqrt{\sum_{i=1}^{N_p}\frac{\left(abs\left(HH_i/HV_i\right)\right)^2}{N_p}}, \sqrt{\sum_{i=1}^{N_p}\frac{\left(abs\left(VV_i/VH_i\right)\right)^2}{N_p}}\right\}\right) \tag{4}$$

The polarization channel amplitude imbalance is defined as the ratio between the HH and VV signal energies of the co-polarized channels. The amplitude imbalance calculation formula is as follows:

$$\Delta_{pol2} = 20\cdot\lg\sqrt{\sum_{i=1}^{N_p}\frac{\left(abs\left(HH_i/VV_i\right)\right)^2}{N_p}} \tag{5}$$

Polarization channel phase imbalance is defined as the difference between the HH and VV signal phases of the co-polarized channels.

The phase imbalance calculation formula is as follows:

$$\Delta_{pol3} = \sqrt{\sum_{i=1}^{N_p}\frac{\left(phase\left(HH_i/VV_i\right)\right)^2}{N_p}} \tag{6}$$

Preprints (www.preprints.org) | NOT PEER-REVIEWED | Posted: 13 October 2023 doi:10.20944/preprints202310.0900.v1

It can be seen from the measurement of the resolution index by multiple calibrators that have traveled many times. The following table shows the calibration results:

Table 7. Polarimetric calibration results.

Parameter	Value
Polarization isolation(dB)	-30.67
Phase imbalance(°)	3.41°
Amplitude imbalance(dB)	0.98dB

In the entire width range, the polarization isolation is better than -30dB, the amplitude unbalance is better than 1dB, and the phase unbalance is better than 5°.

3. Results

On May 24 and 27, 2020, agricultural observation experiments were carried out in Yushu, Jilin Province, and a total of about 1,400 square kilometers (two-way) of S-band full-polarization quantitative data was obtained. The figure below shows the Pauli decomposition image of the same survey area before and after calibration. Agricultural users have carried out research on soil moisture inversion and straw returning, and the accuracy of soil moisture inversion has reached 85%. Through further multi-source, multi-temporal and multi-angle observations, the S-band RCS characteristic curves of different ground objects can be counted, the polarization scattering characteristic matrix can be constructed, the inversion research of bare soil and vegetation-covered soil parameters can be carried out, and the effect of S-band SAR on water, oxygen and other factors can be explored. Explore the ability of S-band SAR to reflect changes in water, oxygen, salinity, etc., and crop growth, and lay a foundation for further exploration of the interaction between S-band electromagnetic waves and ground objects.

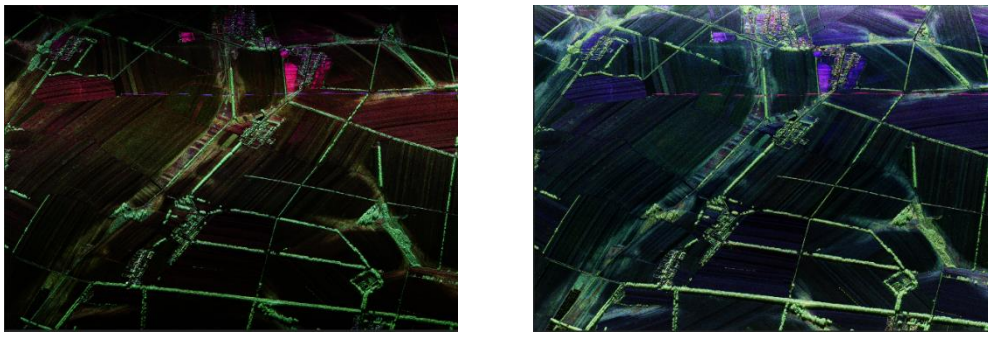

(a) (b)

Figure 7. Quantitative Measurement Effect (Pauli Decomposition) (a) Before the calibration of the elm survey area (b) after the calibration of the elm survey area.

3.1. Agricultural application Experimental

Reference[25] gives the process of Pauli decomposition, and the following three coefficients are obtained by Pauli decomposition:

$$\alpha = \frac{S_{hh} + S_{vv}}{\sqrt{2}} \quad \beta = \frac{S_{hh} + S_{vv}}{\sqrt{2}}, \gamma = \sqrt{2} \cdot S_{hv} \tag{7}$$

The physical meaning of Pauli decomposition: The backscatter process in the case of a single station can be understood as the coherent superposition of three basic mechanisms. α is a single scattering, β is an even scattering with an incident angle of 0 degrees, γ is an even scattering with

Preprints (www.preprints.org) | NOT PEER-REVIEWED | Posted: 13 October 2023 doi:10.20944/preprints202310.0900.v1

a 45-degree inclination angle where all signals are backscattered to the cross-polarized channel, and is dominant for bulk scattering that produces large cross-polarized echoes.

Taking the S-band SAR system as an example, the Pauli decomposition of the area 45.1181°N~45.1250°N,126.5000°E~126.509°E is carried out, and the results shown in Figure 8(a) are obtained, which $|\alpha|^2$ are blue, $|\beta|^2$ are red, and $|\gamma|^2$ are green. The red and blue colors show the predominance of single and even scattering (horizontal and vertical), the blue mainly reflects the even scattering that occurs on the ground and stems of vegetation, and the green hue indicates the predominance of volume scattering. Figure 8(b) is an optical picture in this area. In Figure 8(a), the black soil is in the red box, and its backscatter coefficient is measured. The results are shown in Table 8. The backscattering coefficient obtained in this region is basically consistent with the mean value of the backscattering coefficient given in literature[26], which indicates that the quantization accuracy of the S-band radar system can meet the requirements. Figure 9 shows the measurement point data of agricultural users, combined with the ground synchronous measurement of agricultural users. Table 8 shows the backscatter coefficient and polarization scattering characteristics of the whole straw-covered land, part of the straw-covered land and sprouting land, among which the sprouting land can be considered to be no straw mulch.

(a) (b)

Figure 8. Polarization Scattering Characteristics of Black Soil (a) Black Earth Image (Pauli) (b) Optical Image.

Table 8. Scattering Cross-Sectional Area of Different Land.

Land type	RCS(dB)	Backscatter coefficient(dB)
Black earth	-39.8980	-22.0418
Full straw mulch earth	-23.1334	-7.4075
Partially covered land with straw	-33.6665	-17.2415
Sprouting land	-32.7417	-15.8347

Preprints (www.preprints.org) | NOT PEER-REVIEWED | Posted: 13 October 2023 doi:10.20944/preprints202310.0900.v1

(a) (b) (c)

Figure 9. Surveying Point Map of Agricultural Users (a) Full straw cover land (b) Partial straw cover land (c) Sprouted land.

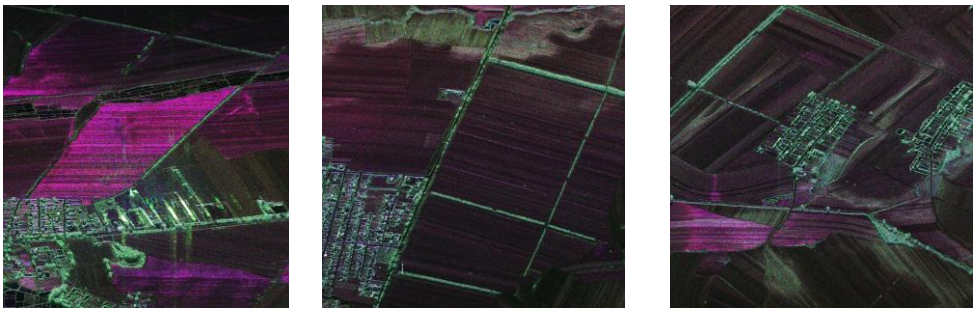

(a) (b) (c)

Figure 10. Scattering Characteristics of Different Land Polarizations (Pauli Decomposition) (a) Full straw covered land (b) Partial straw covered land (c) Open bud land.

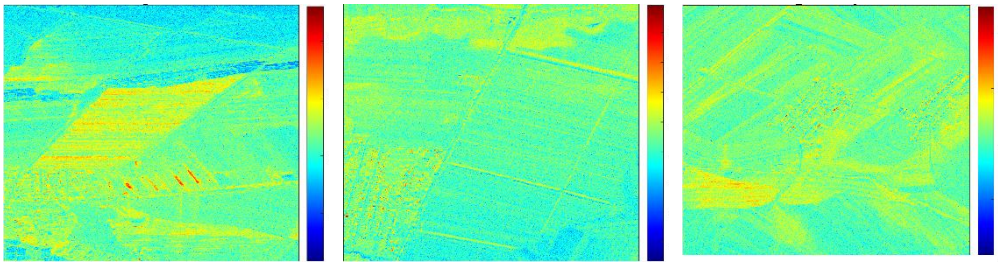

(a) (b) (c)

Figure 11. Backscatter Coefficient Map of Different Land (a) Full straw covered land (b) Partial straw covered land (c) Open bud land.

In this section, the polarization scattering characteristics and backscatter coefficient measurements of different land types are carried out using the data obtained from the flight field experiment. Figure 10 and Figure 11 obtain the polarization scattering characteristics and backscatter coefficients of different soils, and the results shown in Table 8 are obtained. It can be seen that there are differences in the RCS and backscatter coefficients of the land under different coverages. This difference can be used to make statistics on the straw coverage and provide a basis for the classification of land types in the future.

Further experiments were carried out to measure the backscatter coefficient of ground objects. Figure 12 shows the statistical curves of bare land and straw-covered land obtained by the S-band radar respectively. The local jitter is affected by other substrates at this angle.

Preprints (www.preprints.org) | NOT PEER-REVIEWED | Posted: 13 October 2023 doi:10.20944/preprints202310.0900.v1

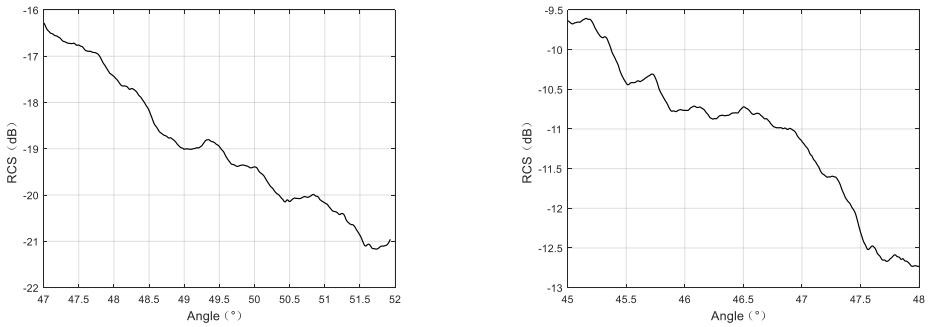

(a) (b)

Figure 12. Backscatter Coefficient of S-Band Black Soil (a) bare black earth (b)straw mulch.

3.2. Multi-Temporal Change Detection, Soil Moisture Inversion

Flight tests were carried out in the area 45.1451N°~45.1807N°,126.5154°E~126.5605°E on 24 May and 27 May 2020, and the polarization scattering characteristic map in this area was obtained. Figure 13(a) shows the partial area polarization scattering characteristic map obtained by Pauli decomposition. Combined with agricultural the user's measuring point data is shown in Figure 13(b), and the backscatter characteristic curve within the same viewing angle range is obtained by measuring this area, as shown in Figure 14.

(a) **(b)** **(c)**

Figure 13. Testing region (a) Land Polarization Scattering Diagram (Pauli Decomposition) (b) User Measuring Point Data.

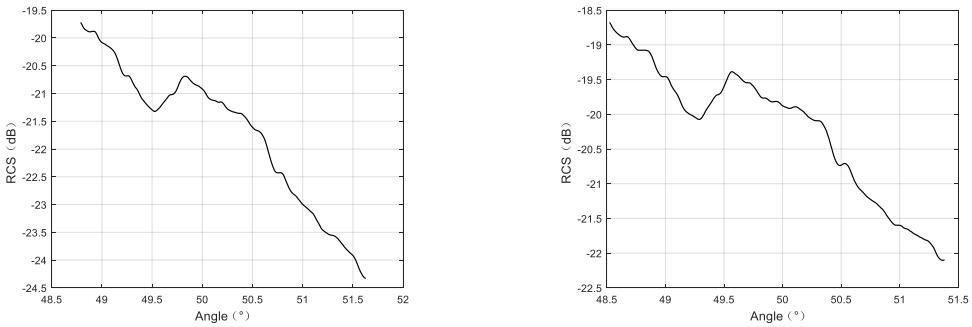

(**a**) (**b**)

Figure 14. Backscatter Coefficient Curve in the Same Area (a) May 24 (b) May 27.

A rain fell between 5.24 and 5.27, which caused changes in soil moisture content, and the backscattering coefficient measured in the S-band can reflect the changes in soil moisture. Figure 14 reflects the difference in the backscatter coefficients of the same land at different times. The same

 doi:10.20944/preprints202310.0900.v1

location is sampled to obtain the differences 1dB~2dB in the backscatter coefficients at different times at the same location, which can be used to reflect the difference in soil water content.

4. Conclusions

This paper reviews the first agricultural application experiment carried out by the S-band subsystem of China's high-marking aviation system. The research results in soil moisture inversion, wheat straw returning detection, ground feature RCS measurement and multi-temporal ground feature change detection are given, and the potential of microwave remote sensing method for agricultural quantitative application is shown.

Author Contributions: Conceptualization, Y.L., L.W., S.Z., X.Z. and J.L.; methodology, Y.L., L.W., S.Z., X.Z. and J.L.; software, Y.L., L.W. and X.Z.; validation, Y.L., L.W. and J.L.; formal analysis, Y.L., L.W., S.Z. and X.Z.; investigation, Y.L., S.Z., X.Z. and J.L.; resources, Y.L., L.W., S.Z. and X.Z.; data curation, Y.L., L.W., S.Z. and X.Z.; writing—original draft preparation, Y.L., L.W. and X.Z.; writing—review and editing, Y.L., S.Z., X.Z. and J.L.; visualization, Y.L., L.W., S.Z. and X.Z.; supervision, Y.L.; project administration, Y.L. All authors have read and agreed to the published version of the manuscript.

Funding: This research received no external funding.

Institutional Review Board Statement: Not applicable.

Informed Consent Statement: Not applicable.

Data Availability Statement: Not applicable.

Conflicts of Interest: The authors declare no conflict of interest.

References

1. Zhang, M.; Meng, J.; Dong, T.; Bingfang, W. U.; Sun, H., Spectral responses analysis of soybean residues. *Journal of Remote Sensing* **2012,** *16* (6), 1993-2002.
2. Holah, N.; Baghdadi, N.; Zribi, M.; Bruand, A.; King, C., Potential of ASAR/ENVISAT for the characterization of soil surface parameters over bare agricultural fields. *Remote Sensing of Environment* **2006,** *96* (1), 78-86.
3. Baghdadi, N.; Zribi, M.; Loumagne, C.; Ansart, P.; Anguela, T. P., Analysis of TerraSAR-X data and their sensitivity to soil surface parameters over bare agricultural fields. *Remote Sensing of Environment* **2008,** *112* (12), 4370-4379.
4. Champagne, C.; Berg, A.; Belanger, J.; Mcnairn, H.; Jeu, R. D., Evaluation of soil moisture derived from passive microwave remote sensing over agricultural sites in Canada using ground-based soil moisture monitoring networks. *International Journal of Remote Sensing* **2010,** *31* (14), 3669-3690.
5. Gherboudj, I.; Magagi, R.; Berg, A. A.; Toth, B., Soil moisture retrieval over agricultural fields from multi-polarized and multi-angular RADARSAT-2 SAR data. *Remote Sensing of Environment* **2011,** *115* (1), 33-43.
6. Narayanan, R. M.; Mielke, L. N.; Dalton, J. P., Crop Residue Cover Estimation using Radar Techniques. *Applied Engineering in Agriculture* **1992,** *8* (6), 863-869.
7. Mcnairn, H.; Duguay, C.; Boisvert, J.; Huffman, E.; Brisco, B., Defining the Sensitivity of Multi-Frequency and Multi-Polarized Radar Backscatter to Post-Harvest Crop Residue. *Canadian Journal of Remote Sensing* **2001,** *27* (3), 247-263.
8. Mcnairn, H.; Duguay, C.; Brisco, B.; Pultz, T. J., The effect of soil and crop residue characteristics on polarimetric radar response. *Remote Sensing of Environment* **2002,** *80* (2), 308-320.
9. Li, K.; Brisco, B.; Yun, S.; Touzi, R., Polarimetric decomposition with RADARSAT-2 for rice mapping and monitoring. *Canadian Journal of Remote Sensing* **2012,** *38* (02), 169-179.
10. Wu, X.; Kumar, V.; Quinlan, J. R.; Ghosh, J.; Yang, Q.; Motoda, H.; McLachlan, G. J.; Ng, A.; Liu, B.; Yu, P. S.; Zhou, Z.-H.; Steinbach, M.; Hand, D. J.; Steinberg, D., Top 10 algorithms in data mining. *Knowledge and information systems* **2008,** *14* (1), 1-37.
11. Mcnairn, H.; Champagne, C.; Shang, J.; Holmstrom, D.; Reichert, G., Integration of optical and Synthetic Aperture Radar (SAR) imagery for delivering operational annual crop inventories. *Isprs Journal of Photogrammetry & Remote Sensing* **2009,** *64* (5), 434-449.
12. Mcnairn, H.; Kross, A.; Lapen, D.; Caves, R.; Shang, J., Early season monitoring of corn and soybeans with TerraSAR-X and RADARSAT-2. *International Journal of Applied Earth Observation and Geoinformation* **2014,** *28*, 252-259.

13. Xu, L.; Li, S.; Deng, Y.; Wang, R., Unsupervised classification of PolInSAR based on improved four-component decomposition. *Remote Sensing Letters* **2014,** *5* (1-3), 295-304.
14. Jiao, X.; Kovacs, J. M.; Shang, J.; Mcnairn, H.; Walters, D.; Ma, B.; Geng, X., Object-oriented crop mapping and monitoring using multi-temporal polarimetric RADARSAT-2 data. *Isprs Journal of Photogrammetry & Remote Sensing* **2014,** *96*, 38-46.
15. Kenduiywo, B. K.; Bargiel, D.; Soergel, U., Higher Order Dynamic Conditional Random Fields Ensemble for Crop Type Classification in Radar Images. *IEEE Transactions on Geoence & Remote Sensing* **2017,** *PP* (8), 1-17.
16. Li, H.; Zhang, C.; Zhang, S.; Atkinson, P. M., Full year crop monitoring and separability assessment with fully-polarimetric L-band UAVSAR: A case study in the Sacramento Valley, California. *International Journal of Applied Earth Observation and Geoinformation* **2019,** *74*, 45-56.
17. Wu; Y.R.; Concept on Multidimensional Space Joint-observation SAR[J]. *Journal of Radars*, **2013**, 2(2): 135-142.
18. Wu, D; Zhou, Q. B.; Chen, Z. X.; LIU,J, Research advances on crop identification using synthetic aperture radar. *Trasanctions of the Chinese Societsy of Agricultural Engineering* **2014,** *30* (16), 10.
19. Li, Z. G.; Yang, P.; Zhou, Q. B.; Wang, Y. L.; Chang, H. F., Research on spatiotemporal pattern of crop phenological characteristics and cropping system in North China Based on NDVI time series data. *Acta Ecologica Sinica* **2009**.
20. Li, Z.; Tang, H.; Peng, Y.; Wu, W.; Chen, Z.; Zhou, Q.; Li, Z.; Zou, J., PROGRESS IN REMOTE SENSING OF VEGETATION PHENOLOGY AND ITS APPLICATION IN AGRICULTURE. *Chinese Journal of Agricultural Resources and Regional Planning* **2012**.
21. Research advances of SAR remote sensing for agriculture applications: A review. *中国农业科学(英文版)* **2019,** *18* (3), 506-525.
22. Arantzazu, L. A.; Jesús, á.-M., On the Added Value of Quad-Pol Data in a Multi-Temporal Crop Classification Framework Based on RADARSAT-2 Imagery. *Remote Sensing* **2016,** *8* (4), 335-335.
23. Xie, Q.; Dou, Q.; Peng, X.; Wang, J.; Lopezsanchez, J. M.; Shang, J.; Fu, H.; Zhu, J., Crop Classification Based on the Physically Constrained General Model-Based Decomposition Using Multi-Temporal RADARSAT-2 Data. **2022**.
24. LIU,Y.B.; LIU,L.; TONG,Z.Y.; YU;Z.J; A Radiometric Calibration and Error Analysis Method for HWRS SAR at S-band[J]. *Journal of Electronics & Information Technology*, **2019**, 41(8): 1946-1951.
25. Cloude, S. R.; Pottier, E., A review of target decomposition theorems in radar polarimetry. *IEEE Transactions on Geoscience & Remote Sensing* **1996,** *34* (2), 498-518.
26. Ulaby, F. T.; Dobson, M. C., Handbook of Radar Scattering Statistics for Terrain. **1989**.